

# Oxygen-mediated high uniform plasticity in $\alpha$ - $\beta$ titanium alloys

Received: 29 December 2024

Accepted: 24 October 2025

Published online: 02 December 2025

 Check for updatesYahui Yang<sup>1</sup>, Xiuxia Wang<sup>1</sup>, Biao Chen<sup>2</sup>, Shenglu Lu<sup>3</sup>, Kaiyue Liu<sup>2</sup>, Shota Kariya<sup>4</sup>, Xianzhe Shi<sup>1</sup>, Xiaozhou Liao<sup>5</sup>, Katsuyoshi Kondoh<sup>4</sup>, Ma Qian<sup>3</sup> ✉ & Jianghua Shen<sup>1,6,7</sup> ✉

Titanium alloys are critically important materials, yet their development has long been constrained by a fundamental trade-off between yield strength and uniform elongation—a more challenging limitation than the conventional strength–ductility trade-off. Here, we present a dual strategy for  $\alpha$ - $\beta$  titanium alloys that transforms high oxygen from an embrittling liability into a powerful performance enabler. First, we leverage high oxygen ( $\geq 0.40\%$ ) to activate prominent pyramidal  $\langle c + a \rangle$  slip in the  $\alpha$ -phase. Second, we engineer a tailored  $\alpha$ - $\beta$  microstructure through alloy design (Ti–O–Fe), laser-based powder bed fusion, and annealing to enable sustained slip transfer across  $\alpha$ - $\beta$  interfaces. The resulting high-strength  $\alpha$ - $\beta$  alloys achieve record uniform elongations: Ti-0.45O-4Fe delivers  $\geq 14\%$  (total:  $\geq 27\%$ ) at yield strengths  $\geq 980$  MPa, and Ti-0.50O-5Fe achieves  $\geq 13\%$  (total:  $\geq 23\%$ ) at yield strengths  $\geq 1075$  MPa. This work simultaneously addresses the yield strength–uniform elongation trade-off and oxygen embrittlement, demonstrating a design paradigm for  $\alpha$ - $\beta$  titanium alloys.

Titanium alloys are advanced, lightweight materials essential for a wide range of critical applications, including aerospace, defence, cryogenic, maritime, chemical, and medical sectors<sup>1,2</sup>. For most of these applications, titanium alloys with high yield strength ( $\sigma_{0.2}$ , resistance to permanent shape change), high uniform elongation ( $\epsilon_{UCL}$ , ability to undergo uniform plastic deformation without strain localization at stresses exceeding  $\sigma_{0.2}$ ), and high fracture toughness ( $K_{IC}$ , damage tolerance) are ideal. In practice, a fundamental trade-off remains: increasing yield strength leads to concurrent reductions in both uniform elongation (Fig. 1a)<sup>3–36</sup> and fracture toughness (Supplementary Fig. 1). Even more concerning, titanium alloys at high yield strengths typically show uniform elongation of just a few percent (Fig. 1a and Supplementary Fig. 2a), although the elongation at break ( $\epsilon_f$ ) may approach 30% (Fig. 1b and Supplementary Fig. 2b). This pronounced degradation of uniform elongation in high-strength titanium

alloy regimes critically compromises structural reliability during service.

This study presents a dual design strategy to address the persistent yield strength–uniform elongation trade-off in  $\alpha$ - $\beta$  Ti alloys—the workhorse of the titanium industry<sup>30</sup>. Successfully resolving this challenge could open promising avenues for obtaining high fracture toughness, as predicted by established correlations with tensile properties<sup>37</sup>. Notably, our conceptual framework also unexpectedly resolves another longstanding challenge: the embrittling effect of high oxygen content. In the following, we first identify the fundamental origins of limited uniform elongation in high-strength  $\alpha$ - $\beta$  Ti alloys before presenting our design concept.

The plastic deformation of titanium and its alloys is mediated by dislocation glide and twinning. In ultra-pure, hexagonal close-packed (HCP) titanium,  $\langle a \rangle$ -type dislocations dominate because their slip

<sup>1</sup>School of Aeronautics, Northwestern Polytechnical University, Xi'an, China. <sup>2</sup>State Key Laboratory of Solidification Processing, Northwestern Polytechnical University, Xi'an, China. <sup>3</sup>Centre for Additive Manufacturing, School of Engineering, RMIT University, Melbourne, Victoria, Australia. <sup>4</sup>Joining and Welding Research Institute, The University of Osaka, Ibaraki, Japan. <sup>5</sup>School of Aerospace, Mechanical and Mechatronic Engineering, The University of Sydney, Sydney, New South Wales, Australia. <sup>6</sup>Shaanxi Key Laboratory of Impact Dynamics and its Engineering Applications, Xi'an, Shaanxi, China. <sup>7</sup>National Key Laboratory of Strength and Structural Integrity, Xi'an, Shaanxi, China. ✉e-mail: [ma.qian@rmit.edu.au](mailto:ma.qian@rmit.edu.au); [j.shen@nwpu.edu.cn](mailto:j.shen@nwpu.edu.cn)

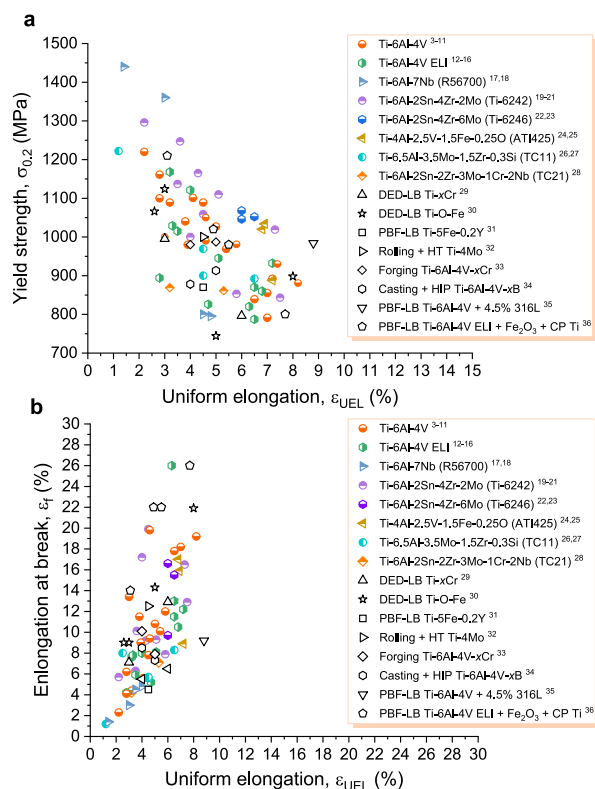


**Fig. 1 | Yield strength ( $\sigma_{0.2}$ ), uniform elongation ( $\epsilon_{UEL}$ ) and elongation at break ( $\epsilon_f$ ) of main  $\alpha$ - $\beta$  titanium alloys.** All strains are engineering strains. **a**  $\sigma_{0.2}$  versus  $\epsilon_{UEL}$  for  $\alpha$ - $\beta$  titanium alloys with  $\sigma_{0.2} \geq 800$  MPa.  $\epsilon_{UEL}$  is roughly inversely proportional to  $\sigma_{0.2}$ . Among these alloys, the PBF-LB Ti-6Al-4V + 4.5% 316 L alloy has the highest  $\epsilon_{UEL}$  of 8.8% ( $\sigma_{0.2} = 984$  MPa), but its elastic modulus ( $E$ ) is only about 80 GPa – typical  $\alpha$ - $\beta$  Ti alloys have  $E = 110$ – $125$  GPa. In addition, the  $\epsilon_{UEL}$  and  $\epsilon_f$  of this alloy are the same, indicating rapid fracture after the onset of strain localization. **b**  $\epsilon_f$  versus  $\epsilon_{UEL}$  for the same  $\alpha$ - $\beta$  titanium alloys in (a), showing the significant difference between  $\epsilon_{UEL}$  and  $\epsilon_f$ . *DED-LB*: laser-based directed energy deposition. *PBF-LB*: laser-based powder bed fusion. *ELI*: extra low interstitial. *HIP*: hot isostatic pressing. *HT*: heat treatment. *CP Ti*: commercially pure titanium.

direction aligns with the closest-packed direction<sup>38,39</sup>. Deformation twinning also readily occurs, accommodating strain along the  $c$ -axis ( $\langle c \rangle$ )<sup>40</sup>. These coordinated mechanisms endow ultra-pure titanium with substantial plasticity ( $\epsilon_f > 75\%$ )<sup>41</sup>, but its yield strength remains undesirably low ( $< 100$  MPa) due to a lack of solid-solution strengthening. To overcome this limitation, alloying—coupled with stringent control of interstitial elements (O, N, C)—has formed the cornerstone of titanium alloy development, including  $\alpha$ - $\beta$  Ti alloys<sup>1,2</sup>.

While effective, this alloying-centered design strategy introduces unforeseen deformation compatibility constraints. The deformation behavior of  $\alpha$ - $\beta$  Ti alloys differs fundamentally from ultra-pure Ti, because alloying elements significantly influence deformation twinning<sup>42,43</sup>. According to the von Mises criterion<sup>40,44</sup>, uniform polycrystalline deformation requires five independent slip systems. However, only four slip systems (two basal and two prismatic)<sup>40</sup> are commonly activated in the  $\alpha$ -phase—all with  $\langle a \rangle$ -type Burgers vectors and none accommodating strain along the  $\langle c + a \rangle$  or  $\langle c \rangle$  directions. Compounding this limitation, the high solute content and small grain size in conventional high-strength  $\alpha$ - $\beta$  Ti alloys typically suppress twinning activity<sup>40,45–47</sup>. The resulting absence of active slip systems in the  $\langle c + a \rangle$  or  $\langle c \rangle$  directions, together with inhibited twinning, severely restricts  $c$ -axis deformation in  $\alpha$ -Ti, ultimately causing poor uniform elongation (Fig. 1a).

To address this fundamental constraint on  $c$ -axis deformation, our solution integrates compositional and microstructural design through a dual strategy: (i) activating pyramidal  $\langle c + a \rangle$  slip via high oxygen content, and (ii) enabling sustained slip transfer through tailored microstructural engineering.

- (i) **Pyramidal slip activation:** We leverage the distinctive ability of high oxygen content to activate second-order pyramidal  $\langle c + a \rangle$  slip in  $\alpha$ -Ti<sup>48</sup>. Oxygen plays a multifaceted role: it provides substantial solid-solution strengthening (760 MPa per 1.0 wt.% O<sup>30</sup>) by impeding prismatic and basal slip<sup>49</sup>, while simultaneously suppressing deformation twinning at concentrations  $\geq 0.20\%$  (all compositions are wt.% unless stated)<sup>42,50</sup>. This suppression of twinning leads to early strain localization and ductility loss, an embrittling effect that intensifies with increasing oxygen content.

Several strategies have been explored to mitigate oxygen-induced embrittlement, including aluminum addition to enhance dislocation cross-slip<sup>51</sup>, the development of entangled  $\alpha$ -Ti phase variants<sup>52</sup>, and the creation of heterogeneous oxygen distributions in  $\alpha$ -Ti<sup>30</sup>. While promising, these methods are typically limited to titanium alloys with oxygen content  $\leq 0.35\%$ , achieving  $\leq 8\%$  uniform elongation at yield strengths  $\geq 800$  MPa. This persistent performance gap underscores the need for a fundamentally different approach.

A review of the literature on tensile deformation of Ti-O alloys reveals that  $\langle c + a \rangle$  dislocation activity is highly sensitive to oxygen content. Whereas one study showed prominent  $\langle c + a \rangle$  activity in Ti-0.4O alloy<sup>53</sup>, another reported primarily  $\langle a \rangle$ -type dislocations in Ti-0.3O alloy<sup>54</sup>. In our previous work<sup>48</sup>, we observed significant  $\langle c + a \rangle$  activation in Ti-0.45O, with even greater prevalence in Ti-0.78O. Collectively, these findings indicate that 0.4% O represents an approximate threshold for substantial  $\langle c + a \rangle$  activation in  $\alpha$ -Ti under high applied stresses ( $> \sigma_{0.2}$ ).

This threshold is underpinned by two complementary mechanisms. First, oxygen strongly suppresses prismatic and basal slip<sup>49</sup> by elevating their critical resolved shear stress (CRSS) values to levels comparable to that required for pyramidal  $\langle c + a \rangle$  slip. Second, oxygen increases the  $c/a$  ratio of  $\alpha$ -Ti<sup>55</sup>, which preferentially reduces the CRSS for pyramidal  $\langle c + a \rangle$  slip relative to prismatic and basal slip systems<sup>56</sup>. These synergistic effects are expected to collectively promote  $\langle c + a \rangle$  dislocation activity in oxygen-stabilized  $\alpha$ -Ti containing more than  $\sim 0.4\%$  O.

To leverage this distinctive effect of oxygen, we incorporated 0.45% O into our target alloys. However, simply adding  $\geq 0.40\%$  O is insufficient—such high-oxygen titanium alloys typically exhibit poor tensile ductility<sup>57–59</sup>. To address this longstanding challenge, we posit that sustaining pyramidal slip after its initial activation is critical. Our strategy is therefore designed to enable such sustained activity and achieve superior mechanical properties.

- (ii) **Pyramidal slip transfer via microstructure design:** In equiaxed high-oxygen Ti-O alloys, oxygen enhances  $\langle c + a \rangle$  dislocation activity within  $\alpha$ -Ti grains<sup>48</sup>. However, effective slip transfer is hindered by high-angle  $\alpha$ - $\alpha$  grain boundaries (GBs), which act as strong barriers (Supplementary Note 1). In contrast, coherent interfaces in lamellar  $\alpha$ - $\beta$  structures permit efficient slip transfer<sup>60</sup>. To exploit this mechanism, we engineer a  $\beta$ -phase mediator to form an alternating  $\alpha$ - $\beta$  lamellar structure that enables sustained slip propagation.

The work of Luster and Morris<sup>61</sup> demonstrates that lamellar thickness is a critical factor for deformation compatibility. Their model, developed for  $\alpha$ - $\gamma$  Ti-Al alloys, predicts enhanced slip system

activation in lamellae thicker than  $\sim 1\ \mu\text{m}$ , where the thickness constrains slip and modifies the local stress state. We posit that this principle extends to  $\alpha$ - $\beta$  Ti alloys, as both systems share key characteristics: lamellar morphologies, coherent interfaces, and similar Burgers orientation relationships (BORs). Specifically, the BOR for the  $\alpha_2$ - $\gamma$  system is  $\langle 11\bar{2}0 \rangle_{\alpha_2} \parallel \langle 011 \rangle_{\gamma}$  and  $(0001)_{\alpha_2} \parallel \{111\}_{\gamma}$ , while for the  $\alpha$ - $\beta$  system it is  $\langle 11\bar{2}0 \rangle_{\alpha} \parallel \langle 111 \rangle_{\beta}$  and  $(0001)_{\alpha} \parallel \{110\}_{\beta}$ . However, increasing lamellar thickness can compromise strength. Therefore, our design targets an  $\alpha$ -phase lamellar thickness of 1–3  $\mu\text{m}$  to balance these competing factors.

Existing theoretical frameworks offer no established guidelines for selecting the optimal  $\beta$ -phase fraction. We therefore consulted empirical data from additively manufactured, strong, and ductile  $\alpha$ - $\beta$  Ti-6Al-4V alloys as a reference. As summarized in Supplementary Table 1, these data indicate a consistent  $\alpha$ - to  $\beta$ -lath thickness ratio of  $3.97 \pm 0.48$ , which corresponds to a  $\beta$ -phase volume fraction of approximately 20%. This ratio thus informed our target  $\beta$ -phase fraction.

Iron (Fe) is the most potent and cost-effective  $\beta$ -stabilizing element, with an intermediate density among common  $\beta$ -stabilizers such as V, Cr, Mo, and Nb. Additionally, laser-based additive manufacturing allows significant alloying with Fe without  $\beta$ -fleck formation<sup>30</sup>. For these reasons, Fe was selected to achieve a 20 vol.%  $\beta$ -phase. Thermodynamic calculations indicate that an addition of 4.0% Fe is required to form 20 vol.%  $\beta$ -phase in the presence of 0.45% O in Ti at room temperature (RT) (Supplementary Fig. 3). Based on these considerations, the target  $\alpha$ - $\beta$  alloy composition was designed as Ti-0.45O-4Fe. The  $\alpha$ - $\beta$  nature of this composition is confirmed through water quenching from the  $\beta$ -phase region, which yields a fully martensitic structure (Supplementary Fig. 4). Conversely, a metastable  $\beta$  alloy would have retained the  $\beta$ -phase after quenching.

With the composition determined, we focus on microstructure control to enable effective pyramidal slip transfer. Our strategy targets two key features: prior- $\beta$  grain morphology and size, and the  $\alpha$ - $\beta$  lamellar structure. Fine, equiaxed prior- $\beta$  grains are desired to enhance structural uniformity and reduce anisotropy<sup>62</sup>. Notably, both oxygen and iron promote the columnar-to-equiaxed transition in titanium alloys<sup>30,63</sup>. Experimentally, we find that shifting from laser-based directed energy deposition (DED-LB,  $10^2$ – $10^5$  °C/s)<sup>30</sup> to laser-based powder bed fusion (PBF-LB,  $10^5$ – $10^7$  °C/s)<sup>64,65</sup> significantly refines equiaxed prior- $\beta$  grains in Ti-0.45O-4Fe. We therefore selected PBF-LB for its ultrahigh cooling rates and superior design flexibility<sup>66</sup>.

Finally, post-PBF-LB annealing is essential to relieve residual stresses, eliminate metastable phases, yield a stabilized  $\alpha$ - $\beta$  lamellar structure, and allow for adjustment of the  $\alpha$  lamellar thickness. Critically, this step also minimizes the initial dislocation density in each phase, as excessive dislocations hinder pyramidal slip activation and transfer. To this end, we conducted a detailed annealing study. As demonstrated in the following section, this integrated design framework yields the target advanced mechanical properties.

## Results and discussion

We prepared spherical Ti-0.41O-3.91Fe powder for PBF-LB (Supplementary Fig. 5). The as-printed alloy compositions ranged from Ti-(0.43-0.46)O-(3.91-3.99)Fe (Supplementary Table 2), hereafter collectively denoted as Ti-0.45O-4Fe. Across all processing conditions (Supplementary Table 3), the microstructure consistently exhibited fine equiaxed prior- $\beta$  grains averaging  $28 \pm 15\ \mu\text{m}$  (Fig. 2a and Supplementary Fig. 5d). Our literature survey indicates that this may be the smallest such grain size reported in bulk  $\alpha$ - $\beta$  titanium alloys<sup>62</sup>. Post-PBF-LB processes (e.g., rapid heat treatment<sup>10</sup>) could potentially enable further refinement of these  $\beta$  grains.

Each equiaxed prior- $\beta$  grain contained ultrafine  $\alpha$ - $\beta$  lamellae ( $87 \pm 24\ \text{nm}$ ), forming a hierarchical structure (Fig. 2b and Supplementary Fig. 6). The matrix consisted of an Fe-poor  $\alpha$ -phase ( $0.5 \pm 0.2\%$

Fe) (Fig. 2c–e), while the secondary phase was an Fe-rich  $\beta$ -phase ( $10.1 \pm 0.8\%$  Fe) (Supplementary Fig. 7 and Supplementary Table 4). We also identified metastable nanoscale  $\omega$ -phase particles (Fig. 2e, f and Supplementary Fig. 8), a feature characteristic of high-iron titanium alloys<sup>67</sup>. The alloy exhibited few pores or microcracks (Supplementary Fig. 5d), demonstrating its excellent PBF-LB processability.

Following our design framework, we annealed the alloy at 600–900 °C for 1 h. At 600 °C, the  $\omega$ -phase persisted (Supplementary Figs. 8, 9), whereas annealing at  $\geq 800$  °C eliminated it (Supplementary Fig. 8). Higher annealing temperatures induced several distinct microstructural modifications: (1) coarsening of  $\alpha$ - $\beta$  lamellae (Fig. 3a, Supplementary Fig. 10 and Supplementary Table 5), (2) precipitation of GB  $\alpha$ -phase (Supplementary Fig. 10), (3) blunting of  $\alpha$ -lamellae (Fig. 3b and Supplementary Fig. 11), and (4) a decrease in  $\beta$ -phase content (Supplementary Table 4). Specifically, increasing the annealing temperature from 800 °C to 900 °C for 1 h caused pronounced coarsening:  $\alpha$ -lath thickness increased from  $2.43 \pm 0.44\ \mu\text{m}$  to  $5.51 \pm 2.26\ \mu\text{m}$ , GB- $\alpha$  width from  $4.68 \pm 1.13\ \mu\text{m}$  to  $7.96 \pm 2.01\ \mu\text{m}$ , and GB- $\alpha$  phase fraction from  $24.2 \pm 2.7\%$  to  $33.3 \pm 3.7\%$ .

Annealing at 800 °C for 1 h yielded a RT microstructure containing 22 vol.%  $\beta$ -phase, determined from the lever rule using measured Fe contents, as well as backscattered electron images (Supplementary Table 4 and Supplementary Fig. 10). The  $\beta$ -phase fraction decreased with higher annealing temperatures (e.g., from 700 °C to 800 °C), a trend driven by changes in the Fe content of the  $\beta$ -phase (Supplementary Note 2). JMatPro simulations predicted a negligible oxygen content in the  $\beta$ -phase (0.001% at 800 °C), thereby concentrating the oxygen in the  $\alpha$ -phase to approximately 0.58%. This elevated oxygen level in the  $\alpha$ -phase is beneficial for activating pyramidal slip under high stress conditions. Previous 3D atom probe tomography (APT) results confirmed minimal oxygen content in the  $\beta$ -phase (0.03 at.%) of a Ti-O-Fe alloy<sup>30</sup>.

Detailed electron backscatter diffraction (EBSD) analysis was performed across a  $3.24 \times 10^4\ \mu\text{m}^2$  area ( $\sim 100$  prior- $\beta$  grains) in the 800 °C  $\times$  1 h annealed Ti-0.45O-4Fe alloy. Both the  $\alpha$ - and  $\beta$ -phases exhibited maximum inverse pole figure (IPF) intensity values below 1.4, confirming negligible microtexturing (Supplementary Fig. 12).

Transmission electron microscopy (TEM) analysis of the 800 °C  $\times$  1 h annealed sample revealed sparse dislocations within individual phases (Fig. 3c), along with clear evidence of dislocation transfer across  $\alpha$ - $\beta$  interfaces (Fig. 3d). In contrast, samples annealed at 600–700 °C retained dislocation-dense  $\alpha$ -regions (Supplementary Fig. 13), which is attributed to insufficient annealing relative to the alloy's high solidus temperature (1665 °C). The resulting  $\alpha$ - $\beta$  lamellae preserved a BOR with coherent interfaces (Fig. 3e).

The as-printed  $\alpha$ - $\beta$  Ti-0.45O-4Fe alloy exhibited an ultrahigh yield strength of  $1560 \pm 7\ \text{MPa}$ , with  $2.3 \pm 0.8\%$  uniform elongation and  $4.5 \pm 0.2\%$  elongation at break (Supplementary Figs. 14, 15). The observed ductility is confirmed by dimpled fracture surfaces (Supplementary Fig. 16a, b). Such tensile properties are unusual for high-oxygen  $\alpha$ - $\beta$  Ti alloys in the absence of thermomechanical processing, underscoring the potential of our approach. The ultrahigh strength originates from synergistic strengthening mechanisms, including solid-solution strengthening from oxygen and iron, nanoscale  $\alpha$ - $\beta$  lamellae (Fig. 2b), high initial dislocation densities (Supplementary Fig. 13), and fine equiaxed prior- $\beta$  grains.

Guided by our design framework, we systematically evaluated the effect of annealing on the mechanical properties of Ti-0.45O-4Fe. Annealing at 600–900 °C for 1 h produced yield strength-uniform elongation combinations (Fig. 4a, b, Supplementary Table 6 and Supplementary Fig. 15) that significantly surpass those of existing  $\alpha$ - $\beta$  alloys (Fig. 1a). Notably, the 800 °C  $\times$  1 h treatment delivered record performance:  $14 \pm 0.3\%$  uniform elongation at  $>980\ \text{MPa}$  yield strength, with a total elongation of  $27 \pm 1.4\%$  (Fig. 4a and Supplementary Table 6). Our literature survey confirms that no other titanium

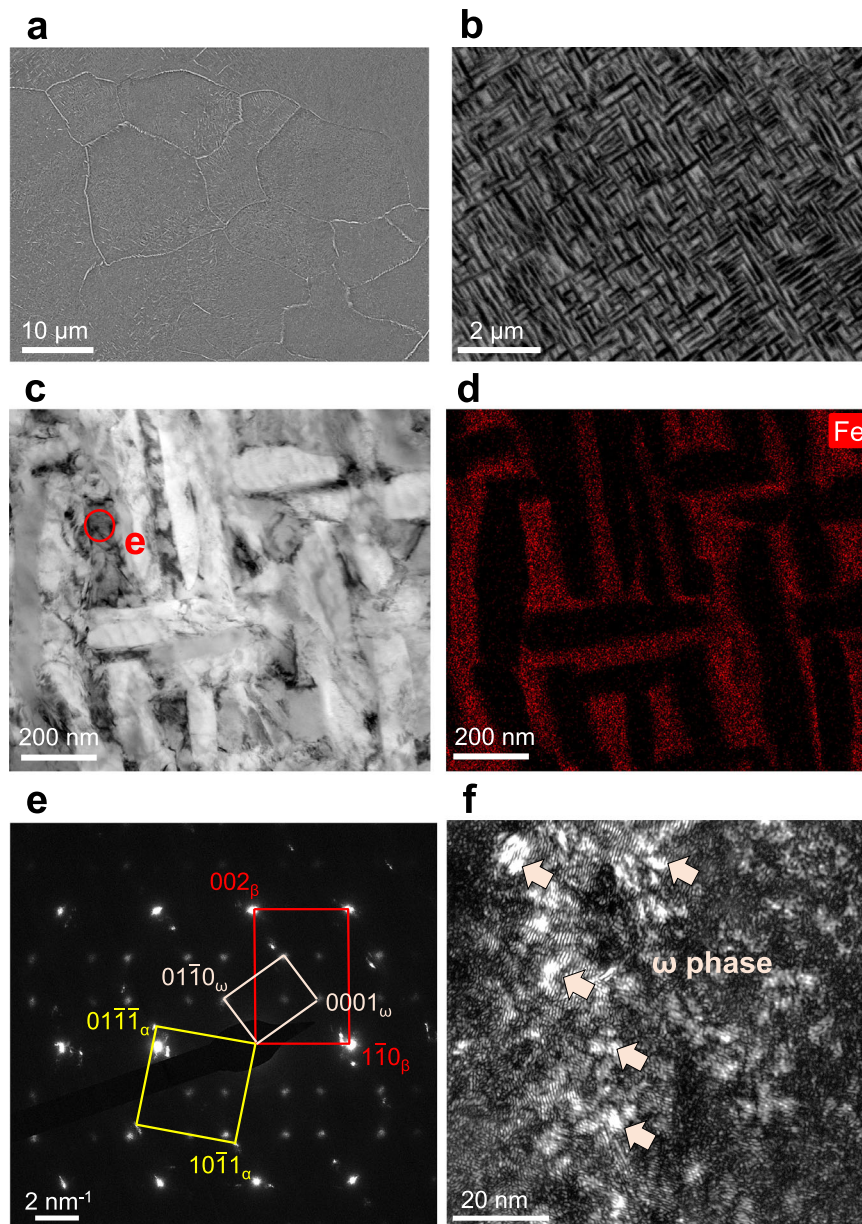


**Fig. 2 | Microstructure of Ti-0.450-4Fe alloy after PBF-LB. a** Scanning electron microscope (SEM) image showing equiaxed prior- $\beta$  grains. **b** Ultrafine lamellar phases in equiaxed prior- $\beta$  grains of (a). **c** A bright-field transmission electron microscope (TEM) view of the ultrafine lamellar phases in (b). **d** Distribution of iron

(Fe) in ultrafine lamellar phases of (c) by energy dispersive X-ray spectroscopy (EDS) mapping. **e** Selected area electron diffraction (SAED) patterns of  $\alpha$ ,  $\beta$ , and  $\omega$  phases in the PBF-LB-fabricated microstructure. **f** A dark-field TEM image of the  $\omega$ -phase precipitates.

alloy has achieved  $\geq 14\%$  uniform elongation at yield strengths  $\geq 900$  MPa—or even  $\geq 800$  MPa—regardless of composition or processing history (Fig. 1a and Supplementary Fig. 2a).

The fracture surfaces of the  $800\text{ }^{\circ}\text{C} \times 1\text{ h}$  annealed alloy exhibit interconnected, aligned fibrous ridges and stretched ligaments bridging elongated dimples (Supplementary Fig. 16e, f). These features are indicative of substantial plastic deformation prior to fracture, which is consistent with the high tensile elongation measured. Remarkably, the strain hardening rates reached 1200–2000 MPa prior to necking (Supplementary Fig. 15c and Supplementary Table 7)—comparable to or even surpassing those of highly ductile 7xxx Al-Zn-Mg alloys (500–1500 MPa) and Fe-C-Mn-Al steels (1000–2000 MPa)<sup>68–71</sup>. This significant strain-hardening capacity reflects extensive dislocation activity, as confirmed by our additional analyses.

In principle, annealing at  $900\text{ }^{\circ}\text{C}$  for 1 h should yield a lower dislocation density than at  $800\text{ }^{\circ}\text{C}$ , potentially enhancing uniform

elongation. However, as Fig. 3c shows, the  $\alpha$ -phase dislocation density after  $800\text{ }^{\circ}\text{C}$  annealing is already minimal, diminishing the expected benefit. Instead, the  $900\text{ }^{\circ}\text{C}$  treatment induced substantial coarsening and pronounced inhomogeneities that hindered uniform deformation. This effect reduced the uniform elongation from  $14.0 \pm 0.3\%$  ( $800\text{ }^{\circ}\text{C}$ ) to  $12.8 \pm 0.5\%$  ( $900\text{ }^{\circ}\text{C}$ ). Despite this slight decrease, the alloy's uniform elongation still significantly surpasses that of conventional  $\alpha$ - $\beta$  Ti alloys (Fig. 1a). These results underscore that maintaining an appropriate microstructural length scale and homogeneity is critical for optimizing performance in this system.

The high tensile ductility of Ti-0.450-4Fe annealed at  $600\text{ }^{\circ}\text{C}$  for 1 h (7% uniform elongation, 16% elongation at break) suggests that its prominent  $\omega$ -phase particles (Supplementary Fig. 9) are most likely the athermal type - known to be non-embrittling in Ti alloys<sup>57</sup>. Since the athermal  $\omega$ -phase is metastable, its subsequent elimination via  $800\text{ }^{\circ}\text{C} \times 1\text{ h}$  annealing enhances microstructural homogeneity and

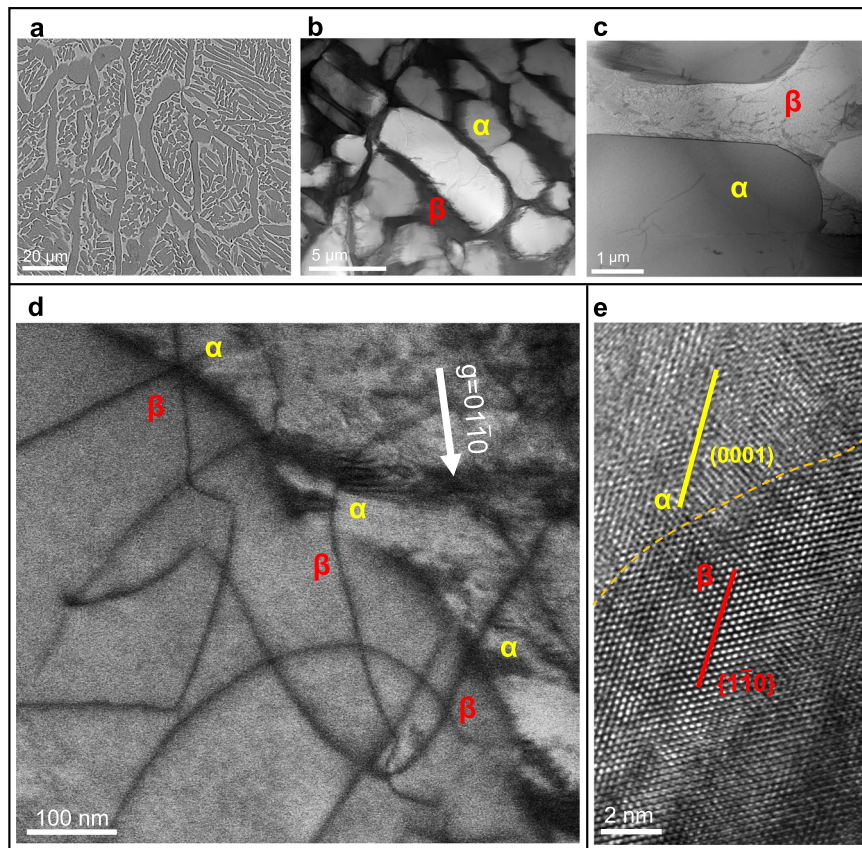


**Fig. 3 | Microstructure of Ti-0.450-4Fe alloy after PBF-LB plus annealing at 800 °C for 1 h. a** Lamellar  $\alpha$ - $\beta$  and grain boundary (GB)- $\alpha$ . The bright phase is the Fe-rich  $\beta$ -phase, while the dark phase is the Fe-poor  $\alpha$ -phase. **b** Blunted  $\alpha$  lamellae after annealing. **c** Only a small number of dislocations were observed in  $\alpha$  and  $\beta$  phases after annealing. **d** Dislocation slip across multiple locations of the  $\alpha$ - $\beta$

interface, photographed for imaging at  $g = \{10\bar{1}0\}$ . **e** Coherent  $\alpha$ - $\beta$  interface. The  $(0001)_\alpha$  plane is parallel to the  $\{110\}_\beta$  plane. The (a) is a back-scattered electron (BSE) image, (b-d) are bright field TEM images, and (e) is a high-resolution TEM image.

stability, thereby improving both uniform elongation and overall ductility.

For comparison, we also processed Ti-0.450-4Fe via ingot casting and forging (Supplementary Fig. 17). In contrast to the PBF-LB alloy, this conventional route produced a coarse, heterogeneous microstructure. This led to constrained ductility ( $\leq 3\%$  uniform elongation;  $\leq 7\%$  total elongation) and significant property variations (Supplementary Fig. 17), underscoring the challenge of achieving reproducible high performance with traditional routes.

Finally, we note that the simultaneous achievement of high uniform elongation and high yield strength is expected to enhance fracture toughness<sup>37</sup>. However, direct experimental measurements are required to confirm this relationship.

To understand the advanced uniform plasticity in high-oxygen Ti-0.450-4Fe alloy, we performed in-situ EBSD tensile testing, focusing on the uniform deformation stage (Fig. 5a and Supplementary Fig. 18). The analysis revealed activation of both prismatic and pyramidal slip (Supplementary Fig. 19), with a distribution of 20% for  $\{10\bar{1}0\}\langle a \rangle$ , 24% for  $\{10\bar{1}1\}\langle a \rangle$ , and 52% for  $\{11\bar{2}2\}\langle c + a \rangle$ . The high oxygen content (0.58 wt.%) in the  $\alpha$ -phase limited basal slip  $(0001)\langle a \rangle$  to just 4%. No  $\{10\bar{1}1\}\langle c + a \rangle$  slip was observed, which is consistent with its higher activation threshold compared to the  $\{11\bar{2}2\}\langle c + a \rangle$  slip<sup>40,43,48,53</sup>.

The predominance of  $\{11\bar{2}2\}\langle c + a \rangle$  slip (52%) validates our design strategy. Elevated oxygen content further promotes activation of  $\{10\bar{1}1\}\langle a \rangle$  slip systems (Supplementary Table 8) by reducing the CRSS ratio of first-order pyramidal  $\langle a \rangle$  to prismatic  $\langle a \rangle$  slip<sup>72</sup>. In situ EBSD during uniform elongation captured extensive slip traces transferring across most  $\alpha$ - $\beta$  interfaces (Fig. 5a and Supplementary Fig. 19a-d),

involving all activated  $\alpha$ -Ti slip systems:  $\{10\bar{1}0\}\langle a \rangle$  (black line) and  $\{11\bar{2}2\}\langle c + a \rangle$  (red line) in Fig. 5a,  $\{10\bar{1}1\}\langle a \rangle$  (blue line) in Supplementary Fig. 19a, and  $(0001)\langle a \rangle$  (purple line) in Supplementary Fig. 19c. Remarkably, long slip traces of 20–30  $\mu\text{m}$ , often spanning 4–10  $\alpha$ - $\beta$  interfaces, were frequently observed (Supplementary Fig. 18g). The  $\{11\bar{2}2\}\langle c + a \rangle$  slip system mediated 57% of slip transfer events (Supplementary Table 9) and 59% of multiple-transfer events ( $\geq 2$  interfaces, Supplementary Table 10). Slip transfer also occurred at interfaces between GB- $\alpha$  and  $\beta$ -phase (Fig. 5a and Supplementary Fig. 19a-d). Collectively, these observations underscore the critical role of  $\{11\bar{2}2\}\langle c + a \rangle$  slip in enabling uniform plastic deformation.

Kernel average misorientation (KAM) mapping confirmed that slip transfer mitigates interfacial strain under high tensile stresses (Fig. 5b). Based on in-situ EBSD data, we calculated the geometric compatibility factors ( $m'$ ) for  $\alpha$ - $\beta$  interfaces in the Ti-0.450-4Fe alloy annealed at 800 °C for 1 h. The values ranged from 0.8 to 1.0 (Table 1, Supplementary Fig. 20a-f), consistent with our observation that slip transfer occurred at nearly all  $\alpha$ - $\beta$  interfaces that adhere to the BOR.

TEM analysis of the Ti-0.450-4Fe alloy annealed at 800 °C for 1 h and tested to 14.2% uniform elongation revealed abundant dislocations in both  $\alpha$  and  $\beta$  phases within the uniformly deformed region (Fig. 5c-f) and the necking zone (Supplementary Fig. 21). Two-beam TEM **g-b** analysis confirmed the predominance of  $\langle c + a \rangle$  dislocations in the deformed  $\alpha$  phase and revealed distinct slip traces traversing  $\alpha$ - $\beta$  interfaces (Fig. 6), validating our  $\langle c + a \rangle$ -dislocation-centered design strategy. The observed increase in hardness from strain hardening (Supplementary Fig. 22), relative to the as-annealed condition, further corroborates this conclusion. No deformation twinning was

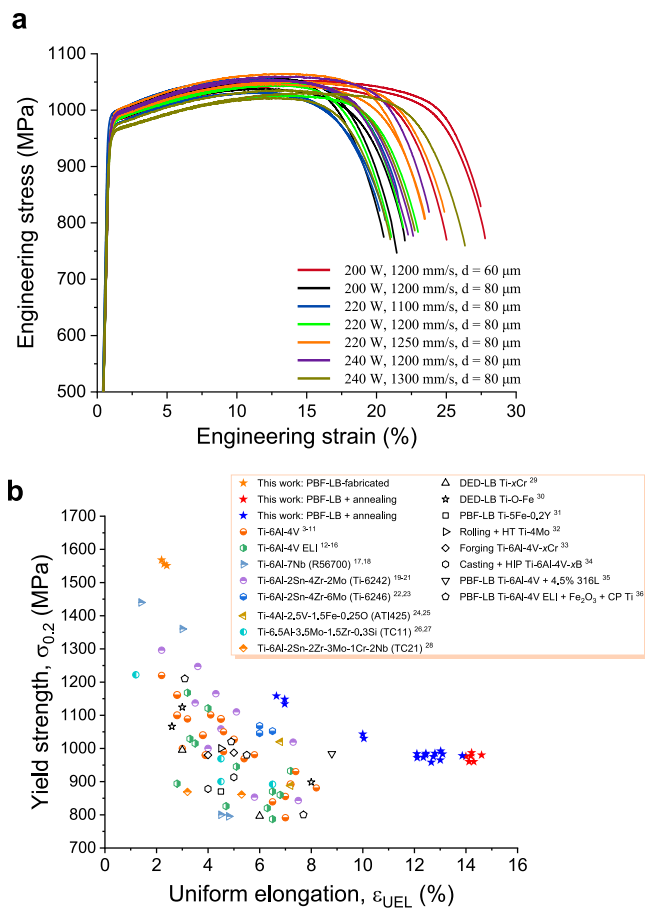


**Fig. 4 | Quasi-static tensile mechanical properties of  $\alpha$ - $\beta$  Ti-0.45O-4Fe alloy at room temperature (RT). **a** Engineering stress–engineering strain curves of  $\alpha$ - $\beta$  Ti-0.45O-4Fe alloy prepared by PBF-LB with different process parameters and subsequently annealed at 800 °C for 1 h. The good reproducibility of these curves causes some overlap. To improve distinguishability, we have set the stress-axis to start at 500 MPa. The symbol d denotes laser spot size. **b** Comparison of tensile yield strength ( $\sigma_{0.2}$ ) versus uniform elongation ( $\epsilon_{UEL}$ ) for  $\alpha$ - $\beta$  Ti-0.45O-4Fe alloy and other  $\alpha$ - $\beta$  titanium alloys. Orange, blue and red solid stars: Ti-0.45O-4Fe alloy (this work). Orange: after PBF-LB. Blue: after PBF-LB + annealing ( $\epsilon_{UEL} < 14\%$ ). Red: after PBF-LB + annealing ( $\epsilon_{UEL} \geq 14\%$ ).**

detected, which is consistent with the high oxygen content in the  $\alpha$ -phase (0.58%).

Beyond microstructural length scale control, achieving high uniform plastic deformation requires minimizing the residual dislocation density in each phase, as specified in our design framework. The reduced uniform elongation (7–10%) observed in alloys annealed at 600–700 °C for 1 h is attributed to their higher residual dislocation densities in both  $\alpha$  and  $\beta$  phases (Supplementary Fig. 13). This same factor also explains the limited uniform elongation ( $\leq 8\%$ ) in recently reported as-printed Ti-(0.35–0.7)O-3Fe alloys<sup>30</sup>. These consistent findings underscore the critical role of post-PBF-LB annealing in microstructural engineering for enhanced uniform plasticity. The specific differences and connections between this study and prior work<sup>30</sup> are outlined in Supplementary Note 3.

It is worth noting that  $\langle c + a \rangle$  dislocations have been reported in the  $\alpha$  phase near  $\alpha$ - $\alpha$  GBs in Ti-0.3 O alloys<sup>54</sup> and at  $\alpha$ - $\beta$  interfaces in Zr-2.5Nb alloy<sup>73</sup> after tensile deformation, although their activation mechanisms remain unclear. In additively manufactured lamellar  $\alpha$ - $\beta$  Ti-O-Fe alloys, recent APT results revealed oxygen enrichment in  $\alpha$ -phase regions adjacent to  $\alpha$ - $\beta$  interfaces, with heterogeneous intragranular distributions from core to periphery within the  $\alpha$  phase, but

no segregation at the  $\alpha$ - $\beta$  interfaces<sup>30</sup>. These observations are consistent with ground-state density functional theory (DFT) predictions of oxygen distribution in both  $\alpha$  and  $\beta$  phases of the same  $\alpha$ - $\beta$  Ti-O-Fe alloys<sup>30</sup>. We propose that such oxygen-enriched  $\alpha$ -phase regions may preferentially activate  $\langle c + a \rangle$  dislocations during early deformation, although this localized effect likely becomes negligible after substantial uniform elongation (e.g., 14.2%, Fig. 6b).

It should be emphasized that slip system alignment alone does not fully determine slip transfer behavior. As shown in Supplementary Table 9, slip transfer can occur more frequently between less-aligned systems than between nearly perfectly aligned ones (e.g.,  $m' = 0.87$  vs.  $m' = 0.98$  for  $\{10\bar{1}0\}\langle a \rangle$ , and  $m' = 0.90$  vs. 0.99 for  $\{11\bar{2}2\}\langle c + a \rangle$ ). These observations suggest that additional factors—such as local stress concentrations and interfacial chemistry (e.g., including the distributions of alloying and interstitial elements)—may also play important roles in governing slip transfer.

Building on these insights, sustaining pyramidal-slip activation and transfer across  $\alpha$ - $\beta$  interfaces under high stress requires a combination of composition and microstructure engineering. The critical prerequisites are: (i) lamellar  $\alpha$  and  $\beta$  phases with coherent interfaces; (ii)  $\alpha$ -laths thick enough ( $>1 \mu\text{m}$ ) to enable activation of multiple slip systems<sup>61</sup>; and (iii) a sufficiently low initial dislocation density to facilitate dislocation motion and minimize hindrance from pre-existing dislocations. Our strategy combines 0.45% O and 4% Fe with optimized PBF-LB processing and post-PBF-LB annealing to achieve the microstructure–property synergy necessary for continuous pyramidal slip. This approach differs fundamentally from equiaxed high-oxygen Ti-O alloys, where high-angle  $\alpha$ - $\alpha$  GBs block slip transfer despite comparable  $\langle c + a \rangle$  activation within  $\alpha$ -phase grains (Supplementary Note 1). These findings demonstrate that microstructural engineering is an equally critical design lever—alongside composition—for controlling deformation pathways in high-strength titanium alloys.

To further validate our design framework, we increased the O content from 0.45% to 0.50% and the Fe content from 4% to 5% according to our design criteria, targeting the Ti-0.50-5Fe composition. The gas-atomized powder composition was Ti-0.470-4.96Fe, with the final PBF-LB-processed and annealed alloy measuring Ti-0.490-5Fe. Tensile properties were evaluated using standard specimens (Methods), while deformation mechanisms were investigated via in-situ EBSD tensile testing.

Relative to Ti-0.45O-4Fe, the Ti-0.50-5Fe alloy exhibited a ~100 MPa increase in yield strength due to intensified solid-solution strengthening (Fig. 7). Importantly, it retained substantial uniform elongation ( $13.2 \pm 0.2\%$ ) and total elongation ( $23.7 \pm 0.2\%$ ) at yield strengths of  $\geq 1075$  MPa, as confirmed by five reproducible stress–strain curves (Fig. 7). The minimal data scatter highlights the alloy's property consistency. Deformation mechanisms closely mirrored those in Ti-0.45O-4Fe (Fig. 8), with 59% of activated slip systems identified as  $\langle c + a \rangle$  slip—quantified across 78  $\alpha$ -phase grains at 10.1% uniform elongation.

These comprehensive results further validate our design strategy of using elevated oxygen content ( $>0.4\%$ ) to activate pyramidal  $\langle c + a \rangle$  slip while enabling effective slip transfer through an engineered  $\alpha$ - $\beta$  microstructure. It is noteworthy that GB- $\alpha$  is prominent in both annealed alloys—Ti-0.45O-4Fe (800 °C  $\times$  1 h) and Ti-0.50-5Fe (900 °C  $\times$  1 h). Although GB- $\alpha$  is often linked to mechanical property degradation, our quantitative EBSD analysis revealed no evidence of GB- $\alpha$  impeding slip transfer (Figs. 5 and 8).

The applicability of our alloy design strategy to other  $\alpha + \beta$  Ti alloys depends on how alternative  $\beta$ -stabilizers affect  $\langle c + a \rangle$  activation in the high-oxygen  $\alpha$ -phase. In the Ti-O-Fe system, Fe's near-zero  $\alpha$ -phase solubility at RT (thermodynamically predicted and APT-confirmed<sup>30</sup>) prevents interference with  $\langle c + a \rangle$  activation. By contrast, conventional  $\beta$ -stabilizers such as V and Mo exhibit measurable

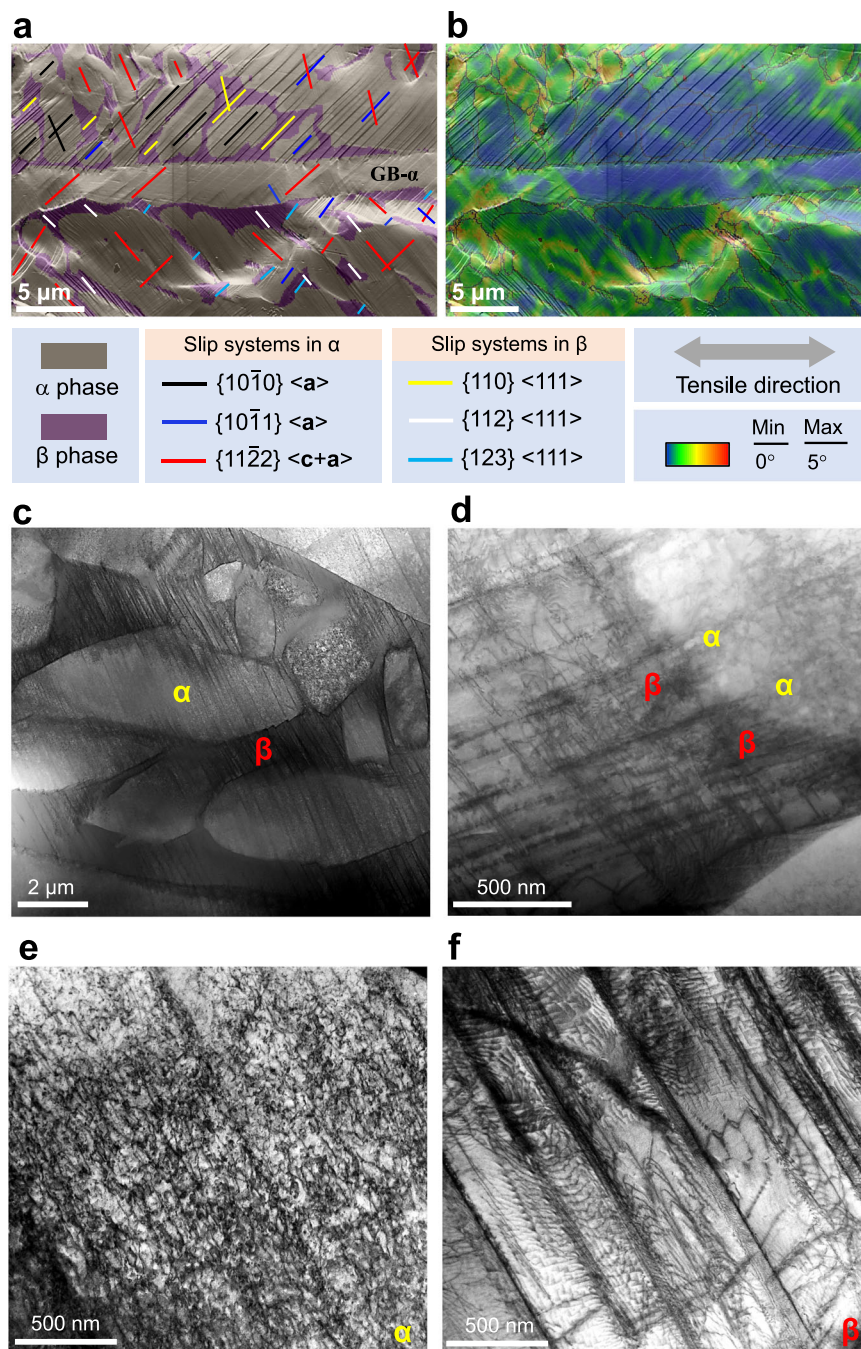


**Fig. 5 | Dislocation activity in  $\alpha$ - $\beta$  Ti-0.450-4Fe alloy (PBF-LB + annealing at 800 °C for 1 h) during tensile deformation.** **a** An SEM image superimposed with the corresponding EBSD phase map, obtained at 14.2% uniform elongation through in-situ SEM uniaxial tensile tests. Multiple slip systems are in operation, the main one being  $\{11\bar{2}\} \langle c + a \rangle$  (red). Slip transfer remained active across almost all  $\alpha$ - $\beta$  interfaces even at 14.2% uniform elongation (true tensile stress  $> 1100$  MPa).

**b** Kernel average misorientation map revealing that slip transfer can effectively relieve strain at many  $\alpha$ - $\beta$  interfaces under high stresses ( $> 1100$  MPa). **c-f** TEM observations after tensile fracture under a two-beam condition to examine dislocations in  $\alpha$  and  $\beta$  phases in the uniformly elongated region ( $\mathbf{g}_\alpha = \{10\bar{1}1\}$  and  $\mathbf{g}_\beta = \{110\}$ ). Massive slip bands traversed multiple  $\alpha$ - $\beta$  interfaces (**c** and **d**), and extensive dislocation multiplication occurred in  $\alpha$  (**e**) and  $\beta$  (**f**) phases.

$\alpha$ -phase solubility (Supplementary Table 11). If these elements hinder oxygen-induced  $\langle c + a \rangle$  activation, complementary strategies—such as Sn alloying<sup>56</sup>, which promotes  $\langle c + a \rangle$  dislocations by increasing the  $\alpha$ -phase  $c/a$  ratio—may be required. Future studies should systematically evaluate the influence of different  $\beta$ -stabilizers on  $\langle c + a \rangle$  dislocation activation to guide advanced titanium alloy design. Moreover, despite segregation-free predictions from ground-state DFT calculations<sup>30</sup>, the possibility of oxygen segregation at  $\alpha$ - $\beta$  interfaces after annealing—and its potential impact on slip transfer through mechanisms such as solute drag requires investigation.

We have demonstrated a framework that overcomes the long-standing trade-off between yield strength and uniform elongation in  $\alpha$ - $\beta$  titanium alloys through two key innovations: (i) leveraging high oxygen content ( $\geq 0.40\%$ ) to activate pyramidal  $\langle c + a \rangle$  slip in  $\alpha$ -Ti, and (ii) engineering an  $\alpha$ - $\beta$  lamellar microstructure via integrated compositional and processing design to sustain slip transfer across phase boundaries.

The resulting compositionally simple Ti-(0.43–0.46)O-(3.91–3.99) Fe alloys deliver record-high performance, achieving  $\geq 14\%$  uniform elongation at yield strengths  $> 980$  MPa and  $\geq 27\%$  total elongation. The

Ti-0.5O-5Fe variant similarly reaches  $\geq 13\%$  uniform elongation at  $\geq 1075$  MPa yield strength with  $\geq 23\%$  total elongation. This dual strategy simultaneously addresses both the yield strength–uniform elongation trade-off and oxygen embrittlement, transforming high oxygen from a liability into a performance-enabling asset.

Our approach opens promising avenues for titanium alloy development, including the use of scrap titanium, recycled high-oxygen powders, or high-purity rutile and ilmenite powders. Moreover, given the analogous effects of oxygen and nitrogen in titanium, this framework could guide the design of  $\alpha$ - $\beta$  Ti-N-Fe alloys with similar performance benefits. Beyond titanium, our interstitial engineering concept may provide a pathway to harness oxygen, nitrogen, and carbon for property optimization across diverse alloy systems, with the potential to catalyze sustainable, low-emission growth in structural materials.

## Methods

### Alloy composition design

According to our alloy design principle, the oxygen content in the  $\alpha$ -Ti phase must be  $> 0.4\%$  to fully activate the  $\langle c + a \rangle$  slip system<sup>48</sup>. However, excessive oxygen may still lead to premature failure of the alloy<sup>50</sup>. Therefore, we choose a total addition of 0.45% O. Given that oxygen

mainly exists in the  $\alpha$ -phase of  $\alpha$ - $\beta$  titanium alloys, and based on the measured volume fraction of the  $\beta$ -phase (22%) in our  $\alpha$ - $\beta$  Ti-0.45O-4Fe alloy designed below, the actual oxygen content in the  $\alpha$ -phase is estimated to be approximately 0.58%.

Similarly, according to our alloy design principle, it is crucial to introduce an appropriate amount of  $\beta$  phase as a mediator to promote extensive slip transfer of dislocations across multiple  $\alpha$ - $\beta$  interfaces. Based on JMatPro 7.0 predictions, under equilibrium conditions, the addition of 4% Fe is expected to produce about 20 vol.%  $\beta$  phase at RT. Therefore, our alloy composition is determined to be Ti-0.45O-4Fe.

### Powder production

First, Ti-0.45O-4Fe alloy ingots were prepared by triple vacuum arc consumable melting using titanium sponge, Ti-32Fe master alloy block and TiO<sub>2</sub> powder in a mass ratio of 86.5:12.5:1. The ingots were subsequently forged at 1100 °C into round bars measuring  $\phi 60 \times 600$  mm. These bars were then gas-atomized into powder using an electrode induction gas atomization (EIGA) system. The produced powders had a normal size distribution (Supplementary Fig. 5a, b) and were sieved to a size range of 20-50  $\mu\text{m}$  for the PBF-LB process, with characteristic diameters of  $Dv(10) = 21.7 \mu\text{m}$ ,  $Dv(50) = 37.8 \mu\text{m}$ , and  $Dv(90) = 60.7 \mu\text{m}$ . The sieved powders were finally placed in a vacuum oven at 110 °C for 6 h to dry for improved flowability. The powder composition is provided in Supplementary Table 2.

### PBF-LB fabrication

A commercial Bright Laser Technologies (BLT, Xi'an, China) S210/S200 system, with a laser spot size of 60/80  $\mu\text{m}$  and a wavelength of 1060–1080 nm, was utilized for the PBF-LB fabrication. The system offers a maximum laser power of 500 W and a maximum scanning speed of 7000 mm/s. Before the operation, the gas circulation system was purged with high-purity argon (99.99%) at a gas flow rate of 45 L/min until the oxygen content in the build chamber was  $< 100$  ppm (purging time  $\geq 30$  min).

A 105 mm  $\times$  105 mm Ti-6Al-4V substrate (20 mm thick) was used as the build plate. The substrate was preheated to 200 °C before PBF-LB. The layer thickness was set to 30  $\mu\text{m}$ , and a rotated scanning strategy of 67° between successive layers was used. The argon gas flow rate was maintained at 4 L/min during the PBF-LB process.

A series of preliminary experiments were conducted to determine the appropriate PBF-LB processing window for our  $\alpha$ - $\beta$  alloys by considering the equivalent volumetric energy density (VED), laser spot diameter, laser power, scanning speed, and hatch spacing. The identified PBF-LB parameters are summarized in Supplementary Table 3.

**Table 1 | Compatibility of active slip systems between adjacent  $\alpha$  and  $\beta$  grains in  $\alpha$ - $\beta$  Ti alloys adhering to the Burgers orientation relationship**

Slip systems in the $\alpha$ -phase	Slip systems in the $\beta$ -phase	Luster-Morris factor $m'$ <sup>a</sup> ( $0 \leq m' \leq 1$ )
(0001) $\langle a \rangle$	{110} $\langle 111 \rangle$	1
	{112} $\langle 111 \rangle$	0.87
	{123} $\langle 111 \rangle$	0.94
{10 $\bar{1}$ 0} $\langle a \rangle$	{110} $\langle 111 \rangle$	0.87
	{112} $\langle 111 \rangle$	1
	{123} $\langle 111 \rangle$	0.98
{10 $\bar{1}$ 1} $\langle a \rangle$	{110} $\langle 111 \rangle$	1
	{112} $\langle 111 \rangle$	0.88
	{123} $\langle 111 \rangle$	0.95
{1122} $\langle c + a \rangle$	{110} $\langle 111 \rangle$	0.90
	{112} $\langle 111 \rangle$	0.99
	{123} $\langle 111 \rangle$	0.99

<sup>a</sup>Note that the  $m'$  value corresponds to the maximum geometric compatibility factor among all possible slip system pairs.

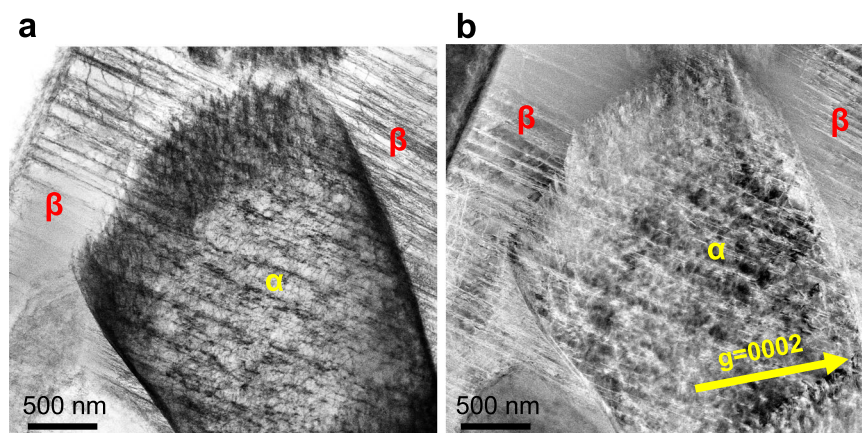


**Fig. 6 | TEM characterization of  $\langle c + a \rangle$  dislocations in the Ti-0.45O-4Fe alloy (PBF-LB + annealing at 800 °C for 1 h) tested to 14.2% uniform deformation. a** Bright-field TEM image. **b** Dark-field TEM image of dislocations observed under two-beam conditions with  $g = (0002)$ .

We printed 22 plate specimens (40 mm × 40 mm × 10 mm) of the Ti-0.45O-4Fe alloy in two batches (Supplementary Fig. 5c), and 36 cylindrical specimens ( $\phi$ 9 mm × 80 mm) of the Ti-0.50-5Fe alloy in a single batch. Following the PBF-LB process, all specimens were allowed to cool to RT inside the build chamber before being removed and detached from the substrate using wire electrical discharge machining.

### Density measurement

Density was determined in alcohol using the Archimedes drainage method (Mettler Toledo- ME204). Before testing, cuboidal specimens (10 mm × 10 mm × 5 mm) were carefully sanded with sandpaper. They were then thoroughly cleaned with alcohol and dried using a cold air blower. Each specimen was measured 10 times at RT to obtain an average value.

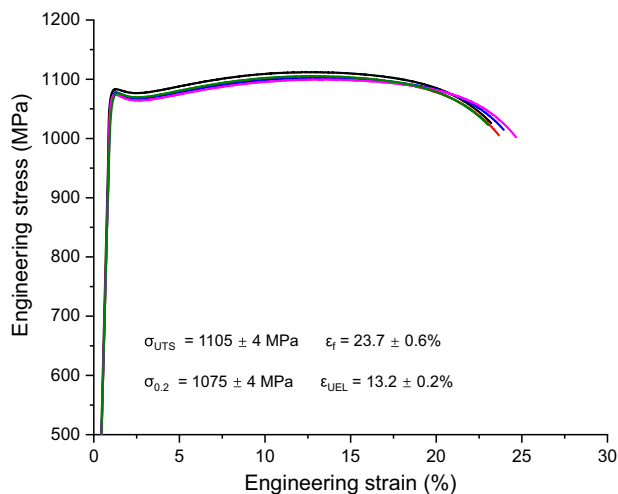


**Fig. 7 | Engineering stress-strain curves of Ti-0.50-5Fe alloy (PBF-LB + annealing at 800 °C for 1 h).** The mechanical properties shown in the inset are derived from five independent stress-strain curves.  $\sigma_{UTS}$ : ultimate tensile strength.  $\sigma_{0.2}$ : yield strength.  $\epsilon_f$ : elongation at break.  $\epsilon_{UEL}$ : uniform elongation.

### Post-PBF-LB annealing treatments

To eliminate metastable phases, relieve residual stresses, and achieve a stable lamellar  $\alpha$ - $\beta$  structure, we annealed our PBF-LB-fabricated Ti-0.45O-4Fe alloy plate samples at 600 °C, 700 °C, 800 °C, and 900 °C for 1 h each, where the  $\beta$ -transus temperature of our alloy is predicted to be 910 °C using the JMatPro 7.0 software. Exceeding this  $\beta$ -transus temperature will result in a coarse Widmanstätten microstructure, which is usually avoided. In contrast, annealing at temperatures below 600 °C typically requires longer times to relieve stress<sup>64</sup>.

All annealing treatments were conducted in a vacuum quartz tube with an inner diameter of 100 mm, which was evacuated to below  $10^{-1}$  Pa prior to heating. The heating rate was 20 °C/min, and the target temperature was maintained for 1 h, followed by furnace cooling. Afterwards, to mitigate potential surface oxidation effects, all annealed samples were polished, despite the high vacuum conditions during annealing.

### Composition analysis

Supplementary Table 1 summarizes the chemical compositions of the powder and specimens after PBF-LB and after PBF-LB plus annealing at 600 °C × 1 h and 800 °C × 1 h. The Fe content was determined using an inductively coupled plasma spectrometer (ThermoFisher-ICAP7600). The O, N, and H contents were measured and confirmed using two ONH analyzers: the LECO-ONH836 from the Center for Analysis and Testing at Northwestern Polytechnical University, and the EMGA-830 HORIBA from the Institute for Joining and Welding Research at The University of Osaka. All measurements were performed in triplicate using approximately 0.5 g of the sample per test. The results obtained from both instruments are consistent (Supplementary Table 2). Prior to chemical composition testing, block samples were sanded to eliminate surface oxidation, then cleaned with alcohol and dried with a cold hair dryer.

### Microstructure characterization

**Scanning electron microscopy (SEM).** A Zeiss Sigma 300 field emission SEM system with an Oxford Nordlys Nano electron backscatter diffraction (EBSD) detector was used for microstructure characterization. Specimens for SEM characterization were ground to 2000# using silicon carbide papers and then electrolytically

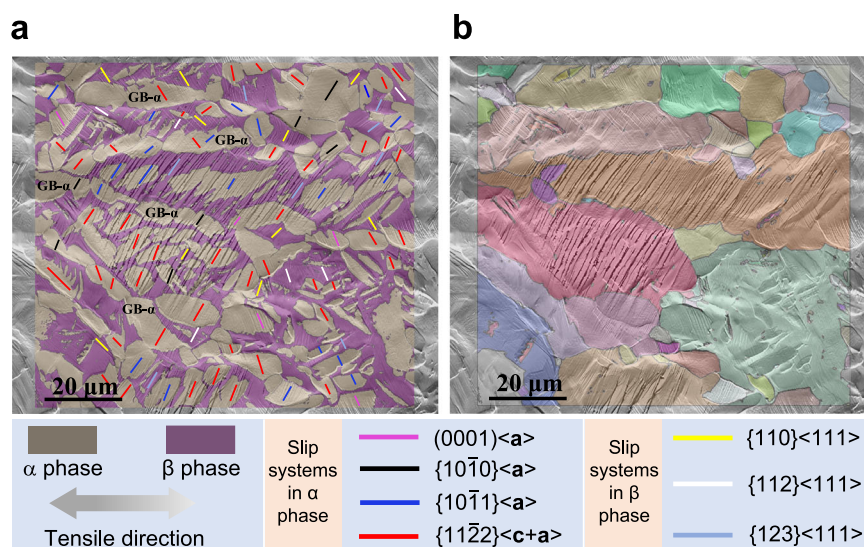


**Fig. 8 | Dislocation activity in  $\alpha$ - $\beta$  Ti-0.50-5Fe alloy (PBF-LB + annealing at 900 °C for 1 h) during tensile deformation.** **a** An SEM image superimposed with the corresponding EBSD phase map, obtained at 10.1% uniform elongation through in-situ SEM uniaxial tensile tests. Multiple slip systems are active, with  $\{11\bar{2}2\}<c+a>$

$a >$  (red) being predominant. **b** Overlaying IPF maps of prior- $\beta$  grains with SEM images reveals numerous slip traces traversing prior- $\beta$  GBs, confirming that GB- $\alpha$  does not hinder slip transfer.

polished at 20 V for 30 s in an electrolytic solution ( $\text{HClO}_4:\text{C}_2\text{H}_5\text{OH} = 1:9$ ) at RT. Specimens were tilted at  $70^\circ$  during EBSD characterization, with a step size of  $0.2\ \mu\text{m}$ , operated at 20 kV. The EBSD data was analyzed using TSL OIM analysis 8 software. All EBSD data are presented in the as-acquired state without any post-acquisition cleanup. Supplementary Table 12 presents the EBSD statistical data, including the hit rate, confidence index (CI), image quality (IQ), and degree of fit. For the overlays of SEM and EBSD images, the transparency of the EBSD component was set to 70%. Furthermore, parent  $\beta$ -grain reconstruction (Supplementary Fig. 12b) was conducted using AZtecCrystal 2.1. The reconstruction employed a voting threshold of  $5^\circ$ —which requires neighboring points to propose a similar parent orientation within this angular tolerance—along with a child threshold of  $5^\circ$  (for  $\alpha$ -phase validation) and a parent threshold of  $10^\circ$  (to define prior- $\beta$  grain boundaries). No data cleanup was performed during this process.

**Transmission electron microscopy (TEM).** TEM characterization was performed using an FEI Talos F200X system, operated at 200 kV. Thin slices ( $\sim 150\ \mu\text{m}$  thick) were prepared from both untested specimens and uniformly deformed regions of tensile-tested specimens using wire-cut electrical discharge machining. These slices were then mechanically thinned from both sides to approximately  $80\ \mu\text{m}$ . Then a TEM-specific punch press was used to make discs of 3 mm in diameter. After that, these discs were first mechanically polished to about  $30\text{--}40\ \mu\text{m}$  thick and then progressively thinned using a precision ion polishing system (Gatan 695 PIPS COOL). The thickness of the region for TEM characterization is less than  $100\ \text{nm}$ .

TEM samples from the necking region after tensile tests were prepared differently. First, the fractured specimen was polished with a series of fine silicon carbide sandpapers (1000#, 2000#, 3000#, 5000#, and 7000#), followed polishing to mirror finish using  $0.04\ \mu\text{m}$   $\text{SiO}_2$  polishing solution. Then, we used an FEI focused ion beam (Helios G4 CX) device to cut about  $100\ \text{nm}$  thick TEM samples located about  $100\ \mu\text{m}$  from the fracture surface, in parallel to the tensile loading direction.

**Energy dispersive X-ray spectroscopy (EDS) data and phase compositions.** The  $\alpha$ -phase and  $\beta$ -phase composition information was obtained through TEM EDS point analysis. To ensure data reliability, we conducted measurements at 20 points from two regions, calculating both the mean and uncertainty. All EDS data (including EDS mapping and point analysis) were collected at an accelerating voltage of 200 kV with a detector acquisition time of 300 seconds.

**Phase fraction quantification.** We used ImageJ 1.53q software to quantify the microstructural features, including the volume fraction of each phase,  $\alpha$ -lamella width, aspect ratio, and bluntness. The  $\beta$  phase volume fraction was determined through the analysis of BSE images using ImageJ 1.53q software. To ensure data reliability and accuracy, we conducted measurements on three distinct regions for each specimen and calculated the average value. Since the accuracy of this method is sensitive to factors such as image noise and resolution—particularly for small features—we manually adjusted the thresholding process to remain as faithful as possible to the original image.

**Slip activation percentage quantification.** We examined four randomly selected regions containing slip traces using combined EBSD characterization, where each region measures  $\sim 1000\ \mu\text{m}^2$  and contain 23–26  $\alpha$ -phase grains. We identified all activated slip systems in these  $\alpha$ -phase grains. The activation percentages represent statistical distributions of each identified slip system. Note that individual  $\alpha$  grains frequently exhibited multiple active slip systems.

## JMatPro predictions

JMatPro 7.0, a material property simulation tool developed by Sentec Software, UK, was used to predict all equilibrium phase transformation temperatures and to evaluate the  $\beta$ -phase fraction at a cooling rate of  $0.5^\circ\text{C/s}$  (similar to furnace cooling) from the single  $\beta$ -phase region (Supplementary Fig. 3). The solidification module was used to calculate the equilibrium distribution of oxygen and iron between the  $\alpha$ - and  $\beta$ -phases in our alloy (Supplementary note 2 and Supplementary Table 11). The results show that the  $\beta$ -phase is essentially free of O, in agreement with experimental observations<sup>30</sup>. As expected, Fe mainly exists in the  $\beta$ -phase.

## Mechanical testing

**Tensile testing.** Quasi-static uniaxial tensile tests were conducted using an Instron 5848 machine equipped with a 2 kN load cell and a non-contact laser extensometer at RT. Dog bone-shaped flat tensile specimens with a gauge of  $1.2\ \text{mm}$  (width)  $\times$   $0.8\ \text{mm}$  (thickness)  $\times$   $8\ \text{mm}$  (length) (as per Chinese Standard GB/T 228.1-2021 and Australian Standard AS 1391-2007) were prepared using wire-cut electrical discharge machining. All tensile specimens were carefully ground using 1000# silicon carbide papers before tensile testing. A nominal strain rate of  $5 \times 10^{-4}\ \text{s}^{-1}$  was applied until fracture occurred. To ensure data reliability, we performed triplicate tensile tests for all sample conditions (Fig. 4a and Supplementary Fig. 14). For the Ti-0.50-5Fe alloy - given its particular significance - we used ISO 6892-1 standard specimens with gauge dimensions of  $\varnothing 5 \times 25\ \text{mm}$ .

**In-situ tensile testing in an SEM system.** Tensile specimens were first sanded with a series of fine sandpapers (1000#, 2000#, 3000#, 5000#, and 7000#) and then polished to a mirror finish using a  $\text{SiO}_2$  polishing solution with a granularity of  $0.04\ \mu\text{m}$  (to avoid corrosion from using a typical chemical polishing solution). The nominal tensile loading strain rate was the same ( $5 \times 10^{-4}\ \text{s}^{-1}$ ). SEM images and EBSD data were acquired at nominal strains of 5%, 10%, and 15%.

**Hardness tests.** After tensile tests, the hardness of the specimens was measured at different distances from the fracture surface using a microhardness tester (HVS-1000A) with a load of 50 g applied for 15 s. Before hardness measurement, the specimens were polished with sandpapers in sequence (1000#, 2000#, 3000#, 5000# and 7000#). The specimen was about  $600\ \mu\text{m}$  thick, the indentation size was less than  $25\ \mu\text{m}$  in length, and the depth was less than  $5\ \mu\text{m}$  (in accordance with the Chinese standard GB/T4342-91). The average value of ten valid measurements was calculated in the corresponding area.

## Slip system identification and statistics

Currently, slip trace analysis combined with EBSD information is the predominant method employed for identifying active slip systems<sup>74</sup>. This approach involves comparing the observed slip traces on the crystal surface (i.e., the intersection of the slip surface with the crystal surface) with predicted slip traces that consider the crystal orientation provided by EBSD<sup>75</sup>. Using this method, the slip systems related to 104 sets of slip traces were determined by comparing them with the corresponding grain plane traces and Schmid factors obtained from Orientation Imaging Microscopy (OIM) analysis 8 (Supplementary Fig. 19).

## Calculation of the $m'$ parameter

A Matlab toolbox developed by D Mercier et al.<sup>76</sup> was used to analyze slip transfer across grain boundaries and to compute the geometric compatibility factor ( $m'$ ). The procedure involved importing EBSD data into the program, defining the relevant slip systems, and subsequently calculating the  $m'$  values at the interfaces. Based on experimental statistics, we focused on three slip systems in the  $\alpha$ -phase,  $\{10\bar{1}0\}\langle a \rangle$ ,

{10 $\bar{1}$ 1}<a>, and {11 $\bar{2}$ 2}<c + a>, and three slip systems in the  $\beta$ -phase, {110}<111>, {112}<111>, and {123}<111>, in our calculations.

## Data availability

Data supporting the findings of this study are available within the article and its Supplementary Information files. Source data are provided in this paper.

## References

- Moiseyev, V. N. *Titanium Alloys: Russian Aircraft and Aerospace Applications* (CRC Press, 2005).
- Welsch, G. et al. *Materials Properties Handbook: Titanium Alloys*, (ASM International, 1993).
- Ren, Y. M. et al. Microstructure and deformation behavior of Ti-6Al-4V alloy by high-power laser solid forming. *Acta Materialia* **132**, 82–95 (2017).
- Xu, W. et al. Additive manufacturing of strong and ductile Ti-6Al-4V by selective laser melting via in situ martensite decomposition. *Acta Materialia* **85**, 74–84 (2015).
- Deconinck, L. et al. In-situ hydrogen embrittlement evaluation of as-built and heat treated laser powder bed fused Ti-6Al-4V versus conventionally cold rolled Ti-6Al-4V. *Addit. Manuf.* **76**, 103768 (2023).
- Lu, S. L. et al. Tailoring hierarchical microstructures to improve the strength and plasticity of a laser powder bed fusion additively manufactured Ti-6Al-4V alloy. *Addit. Manuf.* **71**, 103603 (2023).
- Song, T. et al. Simulation-informed laser metal powder deposition of Ti-6Al-4V with ultrafine  $\alpha$ - $\beta$  lamellar structures for desired tensile properties. *Addit. Manuf.* **46**, 102139 (2021).
- Yvinec, T. et al. Tensile properties of Ti-6Al-4V as-built by laser metal deposition: The relationship between heat affected zone bands, strain localization and anisotropy in ductility. *Addit. Manuf.* **55**, 102830 (2022).
- Zhao, Z. et al. Influence of  $\alpha/\beta$  interface phase on the tensile properties of laser cladding deposited Ti-6Al-4V titanium alloy. *J. Mater. Sci. Technol.* **33**, 675–681 (2017).
- Chong, Y. et al. Mechanical properties of fully martensite microstructure in Ti-6Al-4V alloy transformed from refined beta grains obtained by rapid heat treatment (RHT). *Scr. Mater.* **138**, 66–70 (2017).
- Paramore, J. D. et al. A powder metallurgy method for manufacturing Ti-6Al-4V with wrought-like microstructures and mechanical properties via hydrogen sintering and phase transformation (HSPT). *Scr. Mater.* **107**, 103–106 (2015).
- Kumar, P. et al. Micro- and meso-structures and their influence on mechanical properties of selectively laser melted Ti-6Al-4V. *Acta Mater.* **154**, 246–260 (2018).
- Longhitano, G. A. et al. Correlation between microstructures and mechanical properties under tensile and compression tests of heat-treated Ti-6Al-4V ELI alloy produced by additive manufacturing for biomedical applications. *J. Mater. Process. Technol.* **252**, 202–210 (2018).
- Venkatesh, B. D. et al. Effect of heat treatment on mechanical properties of Ti-6Al-4V ELI alloy. *Mater. Sci. Eng. A* **506**, 117–124 (2009).
- Wang, Z. et al. In-situ SEM investigation on the fatigue behavior of Ti-6Al-4V ELI fabricated by the powder-blown underwater directed energy deposition technique. *Mater. Sci. Eng. A* **838**, 142783 (2022).
- Zhao, Z. et al. Achieving superior ductility for laser solid formed extra low interstitial Ti-6Al-4V titanium alloy through equiaxial alpha microstructure. *Scr. Mater.* **146**, 187–191 (2018).
- Bolzoni, L. et al. Evaluation of the mechanical properties of powder metallurgy Ti-6Al-7Nb alloy. *J. Mech. Behav. Biomed. Mater.* **67**, 110–116 (2017).
- Chlebus, E. et al. Microstructure and mechanical behaviour of Ti-6Al-7Nb alloy produced by selective laser melting. *Mater. Charact.* **62**, 488–495 (2011).
- Galati, M. et al. An investigation on the processing conditions of Ti-6Al-2Sn-4Zr-2Mo by electron beam powder bed fusion: Microstructure, defect distribution, mechanical properties and dimensional accuracy. *Addit. Manuf.* **50**, 102564 (2022).
- Sui, S. et al. Effect of cyclic heat treatment on microstructure and mechanical properties of laser aided additive manufacturing Ti-6Al-2Sn-4Zr-2Mo alloy. *Adv. Powder Mater.* **1**, 100002 (2022).
- Lin, T. et al. Enhanced strength of dual-phase Ti6242 alloy via a heterogeneous microstructure. *Mater. Des.* **230**, 111972 (2023).
- Carrozza, A. et al. A study on the microstructure and mechanical properties of the Ti-6Al-2Sn-4Zr-6Mo alloy produced via Laser Powder Bed Fusion. *J. Alloy. Compd.* **870**, 159329 (2021).
- Hémery, S. et al. Comparison of slip system activation in Ti-6Al-2Sn-4Zr-2Mo and Ti-6Al-2Sn-4Zr-6Mo under tensile, fatigue and dwell-fatigue loadings. *Mater. Sci. Eng. A* **697**, 177–183 (2017).
- Wei, S. et al. In-situ investigation of plasticity in a Ti-Al-V-Fe ( $\alpha$ + $\beta$ ) alloy: Slip mechanisms, strain localization, and partitioning. *Int. J. Plast.* **148**, 103131 (2022).
- Xu, G. et al. Simultaneously improved strength and ductility of low-cost Ti-Al-V-Fe alloy with TiB<sub>2</sub> addition and thermomechanical processing. *Mater. Des.* **232**, 112121 (2023).
- Zhang, B. et al. Geometrical scale-sensitive fatigue properties of Ti-6.5Al-3.5Mo-1.5Zr-0.3Si alloys with  $\alpha/\beta$  lamellar microstructures. *J. Mater. Sci. Technol.* **30**, 1284–1288 (2014).
- Zhu, Z. et al. Achieving high strength in dual-phase Ti-6.4Al-4.4Mo-2.1Zr-0.6Si alloy using cluster formula design. *Mater. Chem. Phys.* **305**, 127938 (2023).
- Ye, X. et al. Effect of aging temperature on mechanical properties of TC21 alloy with multi-level lamellar microstructure. *Mater. Sci. Eng. A* **840**, 142825 (2022).
- Zhang, T. et al. Effect of Cr content on the microstructure and mechanical properties of Ti-Cr alloys manufactured by laser directed energy deposition. *Mater. Sci. Eng. A* **893**, 146143 (2024).
- Song, T. et al. Strong and ductile titanium-oxygen-iron alloys by additive manufacturing. *Nature* **618**, 63–68 (2023).
- Wang, H. et al. Cost-affordable, biomedical Ti-5Fe alloy developed using elemental powders and laser in-situ alloying additive manufacturing. *Mater. Charact.* **182**, 111526 (2021).
- Tarzimoghadam, Z. et al. Microstructure design and mechanical properties in a near- $\alpha$  Ti-4Mo alloy. *Acta Mater.* **97**, 291–304 (2015).
- Boakye, S. Y. et al. A microstructural, mechanical and electrochemical/stress corrosion cracking investigation of a Cr-modified Ti-6Al-4V alloy. *J. Mater. Res. Technol.* **25**, 354–368 (2023).
- Sen, I. et al. Microstructural effects on the mechanical behavior of B-modified Ti-6Al-4V alloys. *Acta Mater.* **55**, 4983–4993 (2007).
- Zhang, T. et al. In situ design of advanced titanium alloy with concentration modulations by additive manufacturing. *Science* **374**, 478–482 (2021).
- Zhang, J. et al. Designing against phase and property heterogeneities in additively manufactured titanium alloys. *Nat. Commun.* **13**, 4660 (2022).
- Schwalbe, K.-H. On the influence of microstructure on crack propagation mechanisms and fracture toughness of metallic materials. *Eng. Fract. Mech.* **9**, 795–832 (1977).
- Rosi, F. D. et al. Mechanism of plastic flow in titanium—determination of slip and twinning elements. *Trans. Am. Inst. Min. Metall. Eng.* **197**, 257 (1953).
- Chong, Y. et al. Ultrahigh yield strength and large uniform elongation achieved in ultrafine-grained titanium containing nitrogen. *Acta Mater.* **240**, 118356 (2022).
- Lütjering, G. et al. *Titanium 2nd* (2007).

41. Ouchi, C. et al. Effects of ultra-high purification and addition of interstitial elements on properties of pure titanium and titanium alloy. *Mater. Sci. Eng. A* **243**, 186–195 (1998).
42. Zaefferer, S. A study of active deformation systems in titanium alloys: dependence on alloy composition and correlation with deformation texture. *Mater. Sci. Eng. A* **344**, 20–30 (2003).
43. Conrad, H. Effect of interstitial solutes on the strength and ductility of titanium. *Prog. Mater. Sci.* **26**, 123–403 (1981).
44. Lee, B. J. et al. On the plasticity of low symmetry crystals lacking five independent slip systems. *Mech. Mater.* **20**, 1–8 (1995).
45. Kang, D. -s. et al. Variation of work hardening rate by oxygen contents in pure titanium alloy. *Mater. Sci. Eng. A* **632**, 120–126 (2015).
46. Christian, J. W. et al. Deformation twinning. *Prog. Mater. Sci.* **39**, 1–157 (1995).
47. Kasemer, M. et al. On slip initiation in equiaxed  $\alpha/\beta$  Ti-6Al-4V. *Acta Mater.* **136**, 288–302 (2017).
48. Shen, J. et al. An in-situ study on deformation and cracking initiation in oxygen-doped commercial purity titanium. *Mech. Mater.* **148**, 103519 (2020).
49. Yu, Q. et al. Origin of dramatic oxygen solute strengthening effect in titanium. *Science* **347**, 635–639 (2015).
50. Yan, M. et al. Review of effect of oxygen on room temperature ductility of titanium and titanium alloys. *Powder Metall.* **57**, 251–257 (2014).
51. Chong, Y. et al. Elimination of oxygen sensitivity in alpha-titanium by substitutional alloying with Al. *Nat. Commun.* **12**, 6158 (2021).
52. Chen, K. et al. Avoiding oxygen-induced early fracture in titanium with high strength via entangled grains through laser powder bed fusion. *Scr. Mater.* **222**, 115051 (2023).
53. Murayama, Y. et al. Effect of oxygen on deformation behavior of texture controlled titanium. *J. Jpn. Inst. Met.* **57**, 628–636 (1993).
54. Chong, Y. et al. Mechanistic basis of oxygen sensitivity in titanium. *Sci. Adv.* **6**, eabc4060 (2020).
55. Chen, B. et al. Advanced mechanical properties of powder metallurgy commercially pure titanium with a high oxygen concentration. *J. Mater. Res.* **32**, 3769–3776 (2017).
56. Wei, S. et al. Discovering pyramidal treasures: multi-scale design of high strength–ductility titanium alloys. *Adv. Mater.* **36**, 2406382 (2024).
57. Luo, S. D. et al. High oxygen-content titanium and titanium alloys made from powder. *J. Alloy. Compd.* **836**, 155526 (2020).
58. Zheng, Y. et al. High strength titanium with a bimodal microstructure fabricated by thermomechanical consolidation of a nanocrystalline TiH<sub>2</sub> powder. *Mater. Sci. Eng. A* **686**, 11–18 (2017).
59. Zhang, C. et al. Vacuum pressureless sintering of Ti-6Al-4V alloy with full densification and forged-like mechanical properties. *J. Mater. Eng. Perform.* **27**, 282–292 (2018).
60. Castany, P. et al. In situ transmission electron microscopy deformation of the titanium alloy Ti-6Al-4V: Interface behaviour. *Mater. Sci. Eng. A* **483–484**, 719–722 (2008).
61. Luster, J. et al. Compatibility of deformation in two-phase Ti-Al alloys: Dependence on microstructure and orientation relationships. *Metall. Mater. Trans. A* **26**, 1745–1756 (1995).
62. Todaro, C. J. et al. Grain structure control during metal 3D printing by high-intensity ultrasound. *Nat. Commun.* **11**, 142 (2020).
63. Simonelli, M. et al. The influence of iron in minimizing the microstructural anisotropy of Ti-6Al-4V produced by laser powder-bed fusion. *Metall. Mater. Trans. A* **51**, 2444–2459 (2020).
64. Laleh, M. et al. Heat treatment for metal additive manufacturing. *Prog. Mater. Sci.* **133**, 101051 (2023).
65. Kobryn, P. A. et al. The laser additive manufacture of Ti-6Al-4V. *JOM* **53**, 40–42 (2001).
66. Yin, J. et al. Dual-beam laser-matter interaction at overlap region during multi-laser powder bed fusion manufacturing. *Addit. Manuf.* **46**, 102178 (2021).
67. Zhou, Q. et al. Laser directed energy deposition of Ti-1Al-8V-5Fe alloy: From zero to significant tensile plasticity. *Scr. Mater.* **239**, 115814 (2024).
68. Zhang, P. et al. Solute cluster evolution during deformation and high strain hardening capability in naturally aged Al-Zn-Mg alloy. *Acta Mater.* **207**, 116682 (2021).
69. Zhi, H. et al. Simultaneously enhancing strength-ductility synergy and strain hardenability via Si-alloying in medium-Al FeMnAlC lightweight steels. *Acta Mater.* **245**, 118611 (2023).
70. Pan, Q. et al. Gradient cell-structured high-entropy alloy with exceptional strength and ductility. *Science* **374**, 984–989 (2021).
71. Wang, X.-Q. et al. Oxygen-gradient titanium with high strength, strain hardening and toughness. *Acta Mater.* **246**, 118674 (2023).
72. Morita, M. et al. Tensile deformation of texture-controlled titanium with high oxygen content at room temperature. *Mater. Sci. Eng.: A* **793**, 139660 (2020).
73. Zou, X.-W. et al. Hierarchical nanolayered structures-enabled record-high fracture resistant zircaloy. *Acta Mater.* **279**, 120300 (2024).
74. Cepeda-Jiménez, C. M. et al. EBSD-Assisted slip trace analysis during in situ SEM mechanical testing: application to unravel grain size effects on plasticity of pure Mg polycrystals. *Jom* **68**, 116–126 (2015).
75. Yang, B. et al. Identification of active slip systems in polycrystals by Slip Trace - Modified Lattice Rotation Analysis (ST-MLRA). *Scr. Mater.* **214**, 114648 (2022).
76. Mercier, D. et al. A Matlab toolbox to analyze slip transfer through grain boundaries. *IOP Conf. Ser. Mater. Sci. Eng.* **82**, 012090 (2015).

## Acknowledgements

This study was supported by the Fundamental Research Funds for the Central Universities supported by the 111 Project of China (No. BP0719007) (J. Shen); the Fundamental Research Funds for the Central Universities (Grant No. D5000210863) (J. Shen); the Key Research and Development Program of Shaanxi Province (2024CY-GJHX-42) (J. Shen); the Australian Research Council (DP220103407) (M. Qian); the OU Master Plan Implementation Project of the University of Osaka (K. Kondoh); and the Environment Research and Technology Development Fund (JPMEERF20213G02) of the Environmental Restoration and Conservation Agency, provided by the Ministry of the Environment of Japan (K. Kondoh). We acknowledge the Analytical and Testing Center of Northwestern Polytechnical University for the facilities and technical assistance, and the scientific and technical support of the RMIT Advanced Manufacturing Precinct and RMIT Microscopy and Microanalysis Facility (RMMF). We extend our gratitude to Zhejiang Tiny Titanium AM Technology Ltd. for their technical support in powder preparation. We thank other team members for their contributions in assisting with data analysis, including Supplementary Fig. 19 (S. Lu), Supplementary Table 5 (M. Li, Z. Du), and Supplementary Table 7 (Y. Zhou).

## Author contributions

Y. Yang completed printing and annealing of samples, mechanical properties testing and analysis, as well as the first draft of the manuscript. Y. Yang and X. Wang completed microstructural characterization and analysis, as well as data visualization. B. Chen provided co-supervision, critically reviewed the results, and edited the manuscript. S. Lu analyzed the microstructure and EBSD data, improved discussions of active slip systems and slip transfer, and critically reviewed the manuscript. K. Liu, X. Shi, X. Liao, S.K., and K.K. critically reviewed the results and edited the manuscript. M. Qian and J. Shen developed the initial concept through discussion with Y. Yang and X. Wang, designed the

experimental alloy, provided detailed supervision to Y. Yang and X. Wang, critically analyzed all experimental data, and completed the manuscript. M. Qian, J. Shen, and Y. Yang led the comprehensive manuscript revision in response to the review comments, addressing all requirements outlined by the journal.

### Competing interests

The authors declare no competing interests.

### Additional information

**Supplementary information** The online version contains supplementary material available at <https://doi.org/10.1038/s41467-025-65851-4>.

**Correspondence** and requests for materials should be addressed to Ma Qian or Jianghua Shen.

**Peer review information** *Nature Communications* thanks Wei-Zhong Han and the other anonymous reviewer(s) for their contribution to the peer review of this work. A peer review file is available.

**Reprints and permissions information** is available at <http://www.nature.com/reprints>

**Publisher's note** Springer Nature remains neutral with regard to jurisdictional claims in published maps and institutional affiliations.

**Open Access** This article is licensed under a Creative Commons Attribution-NonCommercial-NoDerivatives 4.0 International License, which permits any non-commercial use, sharing, distribution and reproduction in any medium or format, as long as you give appropriate credit to the original author(s) and the source, provide a link to the Creative Commons licence, and indicate if you modified the licensed material. You do not have permission under this licence to share adapted material derived from this article or parts of it. The images or other third party material in this article are included in the article's Creative Commons licence, unless indicated otherwise in a credit line to the material. If material is not included in the article's Creative Commons licence and your intended use is not permitted by statutory regulation or exceeds the permitted use, you will need to obtain permission directly from the copyright holder. To view a copy of this licence, visit <http://creativecommons.org/licenses/by-nc-nd/4.0/>.

© The Author(s) 2025